https://doi.org/10.5194/egusphere-2026-565
Preprint. Discussion started: 5 March 2026

Design and evaluation of a catalytic stripper with a plate electrical aerosol classifier

Chengxiang Guo[1,2], Tongzhu Yu[1,3*], Yixin Yang[1*], Huaqiao Gui[1,2,3], Zhe Ji[1,2,4], Jian Wang[3], Jianguo Liu[1,2,5], Wenqing Liu[1,2,3]

[1]Key Laboratory of Environmental Optics and Technology, Anhui Institute of Optics and Fine Mechanics, Hefei Institutes of Physical Science, Chinese Academy of Sciences, Hefei, 230031, China.
[2]University of Science and Technology of China, Hefei, 230026, China.
[3]Institute of Environmental Hefei Comprehensive National Science Center, Hefei, 231299, China.
[4]Key Laboratory of Vehicle Emission Control and Simulation of Ministry of Ecology and Environment, Chinese Research Academy of Environmental Sciences, Beijing 100012, China.
[5]University of Chinese Academy of Sciences, Beijing, 100049, China.

Correspondence to: Tongzhu Yu (tzyu@aiofm.ac.cn) and Yixin Yang (yxyang@aiofm.ac.cn)

Abstract. The catalytic stripper (CS) for removing volatile particles is a critical unit within the measurement system. However, the penetration efficiency of small size particles is currently significantly lower than large particles in CS. Therefore, further improving the penetration efficiency of small size particles is of significant research interest. This study aims to enhance the penetration efficiency of small size particles by reducing the thermophoretic loss. For this purpose, a CS equipped with a plate-type electrical aerosol classifier (EAC) was designed and developed, and its performance was evaluated. The particles are prevented from depositing on the tube wall by applying an electric field force to them in the opposite direction to the thermophoretic force they are subjected to, which ultimately serves the purpose of further improving the particle penetration efficiency. The experimental results demonstrated that the CS achieved a removal efficiency (RE) higher than 99.9% at a flow rate of 1.5 L/min or lower. At a sample flow of 0.3 L/min and a temperature of 350 °C, the penetration efficiency of CS+EAC without voltage was evaluated. Combined with the CS+EAC voltage-penetration efficiency curve, applying -112 V on the EAC, the penetration efficiency was further improved under the same experimental conditions, and the smaller the particle size, the greater the improvement. Compared to the 0 V, the improvement rate for 15 nm at -112 V was 24.4%, while that for 23 nm was 18.9%. Further experimental results show that the EAC can remove particles smaller than 10 or 23 nm by further increasing the voltage. This capability enables rapid particle classification and facilitates high temporal resolution measurements of particle number concentrations across different size intervals.

1 Introduction

Accurately measuring ultrafine particle number concentration (PN) from motor vehicle emissions is essential for the prevention and control of atmospheric particulate pollution (Xie et al., 2023). Mobile source exhaust remains a major source of these emissions. To address this, both the current China VI motor vehicle emission regulations and the forthcoming Euro 7

https://doi.org/10.5194/egusphere-2026-565
Preprint. Discussion started: 5 March 2026

regulations have set clear performance criteria for PN detectors (Liu et al., 2019; Hooftman et al., 2018). Studies have found that a significant portion of some motor vehicle particle emissions comprises particles smaller than 23 nm, with those between 10 and 23 nm representing the higher proportion (Giechaskiel & Martini, 2013; Rönkkö et al., 2014). In response, the latest Euro 7 emission regulations have lowered the particle size detection threshold from 23 to 10 nm and introduced updated standards for exhaust gas pretreatment and particle counting devices (Giechaskiel, 2021).

The ultrafine particles emitted by motor vehicles include volatile and semi-volatile particles, which significantly affect the accurate measurement of non-volatile particles in the exhaust. These volatile and semi-volatile particles can condense to nucleate or attach to non-volatile ones, altering the particle size distribution and number concentration of non-volatile particles. Therefore, according to the national motor vehicle emission standards, the volatile and semi-volatile particles are first removed from the exhaust to minimize their impact on the measurement results, after which the number concentration of non-volatile particles is measured (Melas et al., 2020). Worldwide, real-time measurement of motor vehicle PN emissions relies on exhaust gas sampling pretreatment devices combined with particle counting devices (Giechaskiel, 2019). The exhaust gas pretreatment devices—referred to as volatile particle removers (VPRs) in laboratory systems—fall into three types: evaporation tubes (ETs) that use dilution (Giechaskiel & Drossinos, 2010), thermodenuders (TDs) that remove particles via activated carbon adsorption (Faulhaber et al., 2009; Burtscher et al., 2001; Wehner et al., 2002; Fierz et al., 2007; Park et al., 2008; Huffman et al., 2008; Stevanovic et al.,2015; Louvaris et al., 2017; Babar et al., 2020; Giechaskiel et al., 2014), and catalytic stripper (CS) that operates through catalytic oxidation (Centre et al., 2014; Giechaskiel et al., 2020; Woo et al., 2021; Swanson et al., 2013; Swanson & Kittelson, 2010).

The earlier Euro 6 and China 6 motor vehicle emission regulations have specified the design and performance criteria for the VPR, which comprises a primary diluter, an ET, and a secondary diluter. The primary diluter must achieve a dilution ratio (DR) exceeding 10 and operate at a heating temperature greater than 180 °C. The ET temperature is greater than 350 °C and is used to vaporize volatile and semi-volatile particles into their gaseous state (Giechaskiel & Drossinos, 2010). The two-stage cold dilution cools the high-temperature exhaust gasses to the normal temperature without requiring a specific DR. By lowering steam saturation, it effectively prevents the re-nucleation of volatile and semi-volatile compounds, facilitating their removal. The ET method relies on a higher DR to remove these volatile and semi-volatile particles; however, this reliance can lead to re-nucleation downstream of the VPR, potentially leading to erroneous measurement results (Melas et al., 2020).

To mitigate the issue of re-nucleation, two advanced VPR devices have been developed and implemented: the first is a TD based on activated carbon adsorption (Burtscher et al., 2001; Fierz et al., 2007; Luís et al., 2016; Babar et al., 2020), and the second is a CS that utilizes the catalytic oxidation of precious metals (Jacob et al., 2010; Amanatidis et al., 2018; Melas et al., 2020; Giechaskiel et al., 2020). TD comprises two main components: a desorber tube and an adsorber tube. The desorber tube heats the exhaust gas to 350 °C, converting the volatile and semi-volatile particles into their gaseous state. While this method effectively adsorbs and removes volatile particles, it requires frequent replacement of the activated carbon. Additionally, the TD is large in size, making it difficult to meet the needs of portability and integration. The CS features an internally integrated catalytic oxidizer based on a compact cordierite honeycomb coated with platinum-group noble metals. As volatile particles

https://doi.org/10.5194/egusphere-2026-565
Preprint. Discussion started: 5 March 2026

pass through CS, they undergo catalytic oxidation reactions, converting into CO2 and H2O, which are completely removed. The CS core module is highly compact, and its structure allows for easy integration, enhancing portability and maximizing the efficiency of volatile particle removal.

Based on the following points: (i) the concentration of emitted particles is higher in the 10-23 nm particle size range; (ii) ET and TD cannot completely remove volatile particles and often regenerate volatile particles smaller than 23 nm downstream of them. Therefore, the Euro 7 emissions regulations identify CS—known for their extremely high efficiency in removing volatile particles—as the only approved option for portable emission measurement systems (Giechaskiel et al., 2021). However, the CS exhibits lower particle penetration efficiency compared to devices such as ET or TD, primarily due to its unique honeycomb structure (Giechaskiel et al., 2014). The penetration efficiency of CS primarily depends on particle diffusion loss and thermophoresis loss. Additionally, an inverse correlation exists between the CS' particle penetration efficiency and its volatile particle removal efficiency (RE), whereby enhanced RE results in lower penetration efficiency (Woo et al., 2021). Consequently, improving penetration efficiency is of significant research interest, as it would increase the flexibility in CS parameter design—enabling optimization of the volatile particle RE while maintaining compliance with regulatory standards for CS penetration efficiency.

In volatile particle removal devices, particle losses primarily arise from diffusion losses driven by Brownian motion, and thermophoretic effects caused by heat conduction from the tube center to its wall during exhaust gas cooling. Diffusion losses decrease with increasing particle size, while the thermophoretic losses can be mitigated by reducing the temperature gradient. Based on the analysis of the particle loss mechanisms, the particle penetration efficiency is enhanced by introducing a counteracting force to the thermophoretic effect, thereby reducing particle deposition on the pipe wall. In contrast to the bidirectional thermophoretic force, the electric field force is unidirectional, with its orientation determined by the polarity of the applied high voltage. Therefore, assuming that high-temperature particles enter the electric field from one side of the upper pole plate, particle loss due to thermophoresis can be reduced by applying an electric field force to the charged particles that oppose the thermophoresis force acting on them.

The main electromigration-based classifiers are primarily categorized into electrostatic precipitation (ESP) (Hinds, 1999), electrical aerosol classifier (EAC) (Liu et al., 1976), and differential mobility analyzer (DMA) (Whitby et al., 1966; Liu & Pui, 1975; Knutson & Whitby, 1975). Each type varies in different classification effects and transfer functions. The ESPs tend to have higher particle losses, while the DMAs provide the most accurate particle classification. However, the high cost and complexity of DMAs limit their use in applications where moderate screening effects and lower costs are preferable. Although the EAC offers lower particle size resolution than the DMA, its simple structure and lower cost make it suitable for enhancing particle penetration efficiency in this study (Chen et al., 2018).

Based on the analysis of CS and EAC, this study presents a novel approach by integrating a plate-type EAC downstream of a CS. The EAC generates an electric field force that counteracts the thermophoretic force acting on high-temperature charged particles, reducing their tendency to migrate toward the tube wall. This mechanism enhances particle penetration efficiency without compromising the removal of volatile particles. Further, by analyzing the relationship between the electric field

https://doi.org/10.5194/egusphere-2026-565
Preprint. Discussion started: 5 March 2026

strength and the particle electromobility, the system can achieve precise classification of particles larger than 10 or 23 nm. This configuration enables alternating measurements with a cut-off diameter of 10 or 23 nm, which is crucial for achieving accurate PN measurements.

The remainder of the paper is organized as follows. Section 2 describes the principle and experimental setup; Section 3 presents the results and discussion; and Section 4 concludes the study.

2 Principle and experimental setup

2.1 Design of CS+EAC

The structure of the CS+EAC developed in this study is presented in Fig. 1. The device comprises a stainless-steel CS on the left side and a plate-type EAC on the right side. The CS is fully sealed using welds and graphite gaskets. Positioned at the rear of the CS chamber is the core module—a 40 mm long, 25 mm diameter cordierite honeycomb (200 cells/in^2, cpsi) coated with platinum-group precious metals. The CS is equipped with a 200 W heating jacket that raises and maintains its temperature at 350°C, enabling the removal of volatile aerosol particles. The remaining high-temperature solid particles then flow into the EAC. The left side of the EAC is directly connected to the CS outlet, with a graphite gasket ensuring a sealed interface. The CS outlet aligns with the EAC's sample flow inlet. The EAC receives sheath flow from a side inlet, where a steel mesh at the back end helps establish laminar flow conditions. The high-voltage electrode board in the EAC classification area is a gold-plated FR-4 circuit board, with the following dimensions: 60 mm in length and 20 mm in width, as shown by the blue area in the EAC section of Fig. 1.

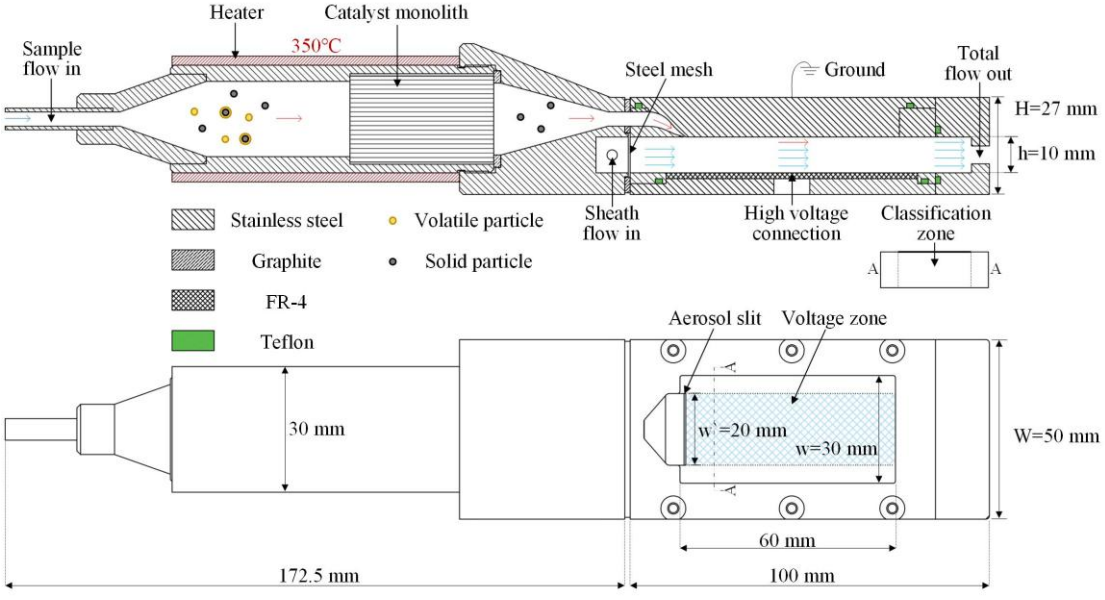

Figure 1: Structure of the integrated CS+EAC system.

https://doi.org/10.5194/egusphere-2026-565
Preprint. Discussion started: 5 March 2026

To minimize the influence of particle diffusion on the classification performance, the EAC flow field is designed to be 10 mm wider than the electric field. The high-voltage wire is welded to the back of the electrode using high-temperature solder wire, and the joint is sealed with high-temperature silicone to prevent leakage. In addition, the electrode side of the circuit board is manufactured without holes, reducing the risk of particle generation from the solder heat and subsequent contamination of the EAC. The high-temperature particles entering the EAC experience two forces: a thermophoretic force along the direction of decreasing temperature and an electric field force that pulls them toward the high-voltage electrode. Increasing the electric field force counteracts the thermophoretic force, thereby progressively reducing the particle thermophoretic losses. Ultimately, the combined sample and the sheath flows exit the EAC. Overall, the CS+EAC system removes, dilutes, and cools volatile particles in the aerosol, while the applied voltage enhances the penetration efficiency of solid particles.

2.2 Theoretical analysis of CS+EAC voltage-penetration efficiency curves

Based on the force and motion trajectory of particles in the flow field and electric field, this study established a two-dimensional flow field model of the EAC and simulated its flow field using COMSOL. Since the aerosol inlet slit is the same width as the particle grading zone, the center profile of the flow field is used as the 2D model. Figure 2 shows the simplified schematic of the EAC's classification region in 2D rectangular coordinates, where x and y indicate the horizontal and rectangular coordinates, respectively. The sheath flow flows along the x -direction, while the aerosol flow cuts into the flow field from $y = 0$ keeping an angle. The simulation parameters are set to the sample flow Q_{sa} = 0.3 L/min and the sheath flow Q_{sh} = 0.9 L/min. Due to the lack of CS, the sample inlet is set to an idealized temperature of 350 °C, which is the heating temperature of CS. The simulated temperature distribution is shown in Fig. 2. It can be seen that particles at different positions at the entrance of the sample flow slit may be subjected to thermophoresis forces in different directions. Particles approaching the grounding plate and entering the classification region are subjected to thermophoresis forces directed toward the grounding plate. Particles approaching Q_{sh} and entering the classification region are subjected to thermophoresis forces directed toward the high-voltage plate. This is due to the sheath flow temperature being lower than the sample flow temperature. As the particles continue moving along the x -axis under the influence of the applied electric field force, similarly, due to the lower temperature of the sheath flow, the particles will be subjected to thermophoretic forces directed toward the high-voltage plate. Based on simulation results, the following theoretical analysis of particles is conducted:

F_{th} represents the thermophoretic force (Talbot et al., 1980), which can be expressed as follows:

$$F_{th} = \frac{3\pi\mu^2 d_p H \nabla T}{\rho_g T}, \quad (1)$$

where μ implies the gas viscosity; d_p refers to the particle size; H denotes the thermophoretic coefficient; ρ_g signifies the gas density; and T denotes the absolute temperature of the particle. Particles acquire a thermophoretic velocity V_{th}, while simultaneously being subjected to a drag force (also known as resistance) in the opposite direction of V_{th}. The drag force can be expressed as

https://doi.org/10.5194/egusphere-2026-565
Preprint. Discussion started: 5 March 2026

$$F_{drag} = -\frac{3\pi\mu d_p V_{th}}{C_c}\,, \tag{2}$$

$$F_{drag} + F_{th} = 0\,, \tag{3}$$

Where C_c denotes the Cunningham correction factor. With Eqs. (1) - (3), V_{th} is expressed in the form:

$$V_{th} = \frac{\mu H \nabla T C_c}{\rho_g T} = F_{th} * \frac{C_c}{3\pi\mu d_p}\,, \tag{4}$$

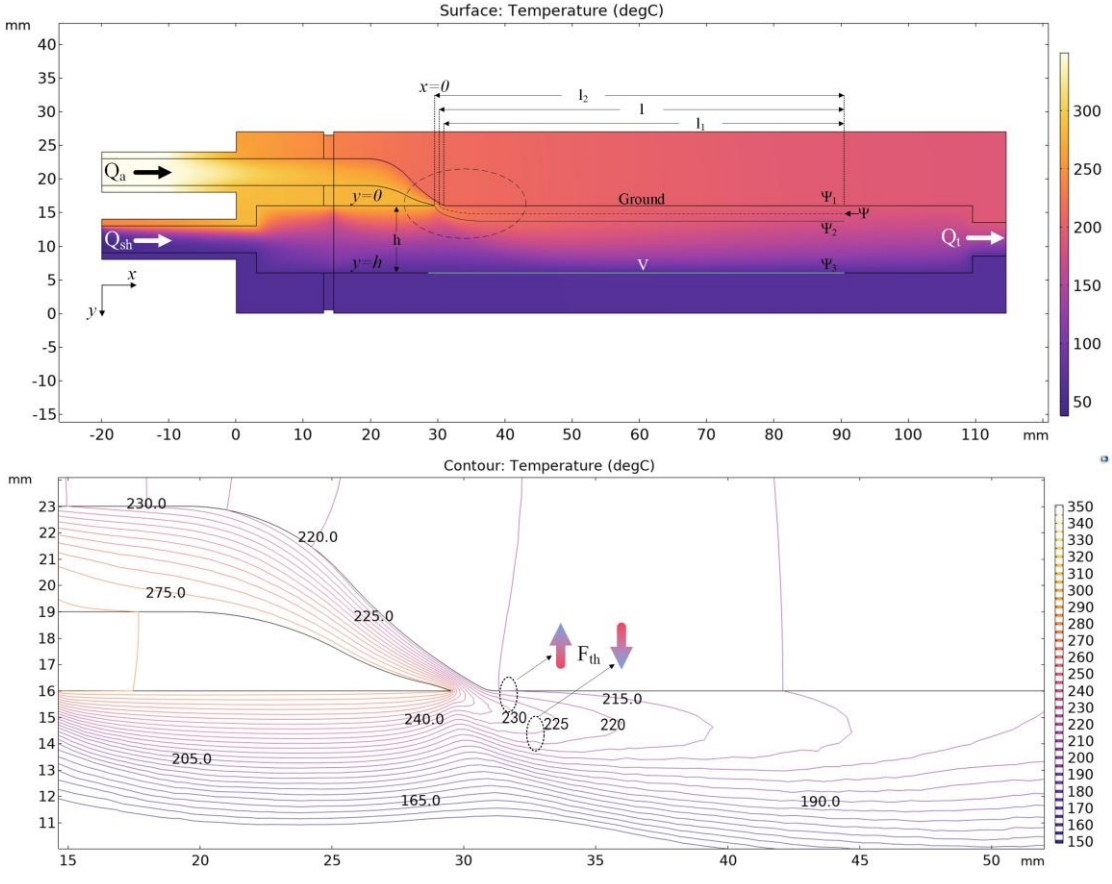

Figure 2: 2D simulation of CS+EAC showing the flow field lines in the particle classification region.

Neglecting the particle gravitational settling, the trajectory of the charged particles under the applied voltage in the EAC is expressed as follows:

$$Z_p = \frac{neC_c}{3\pi\mu d_p}\,, \tag{5}$$

$$\frac{dx}{dt} = u_x\,, \tag{6}$$

$$\frac{dy}{dt} = u_y + Z_p E_y + V_{th} = u_y + \frac{Z_p}{ne} F_{e-y} + \frac{C_c}{3\pi\mu d_p} F_{th} = u_y + \frac{Z_p}{ne}\left(F_{e-y} + F_{th}\right)\,, \tag{7}$$

where Z_p refers to the electric mobility of charged particles; n indicates the number of elementary charge units; e implies the elementary charge unit (1.6×10^{-19}C); u_x denotes the velocity of particles subjected to the fluid traction in the horizontal

https://doi.org/10.5194/egusphere-2026-565
Preprint. Discussion started: 5 March 2026

direction; u_y implies the velocity of particles subjected to the fluid traction in the vertical direction; $Z_pE_y + V_{th}$ indicates the velocity of particles subjected to the vertical component of the electric field force and the thermophoretic force; and $F_{e-y} = E_y ne$ indicates the electric force in the y -direction. For simplicity in theoretical calculations, the electric and flow field distortions within the EAC are disregarded. Furthermore, once the flow temperature stabilized, the F_{th} of all high temperature particles is considered to be a constant and all pointing in one direction.

Based on the theoretical analysis of the EAC voltage-penetration curve, the thermophoretic force is incorporated into the derived equation to model the voltage-penetration efficiency of the CS+EAC at high temperature. The resulting modified particle stream function can be expressed as follows:

$$\Gamma_{(x,y)} = \psi_{(x,y)} + \frac{Z_p}{ne}\left(\Phi_{(x,y)} + \mathrm{T}_{(x,y)}\right), \tag{8}$$

$$\Phi(x,y) + \mathrm{T}(x,y) = \int -F_{e-y} - F_{th} d_x, \tag{9}$$

$$\Delta\psi(x,y) = -\frac{Z_p}{ne}\left[\Delta\Phi(x,y) + \Delta\mathrm{T}(x,y)\right], \tag{10}$$

where ψ refers to the fluid stream function, Φ indicates the electric field force function, and T refers to the thermophoretic force function. Based on Liu's analysis of the fluid stream function (Liu et al., 2016), Eqs. (13) and (14) in his study are modified as follows:

$$\Delta\Phi + \Delta\mathrm{T} = \int_{x_{in}}^{l_2} -F_{e-y} - F_{th} d_x = \left(-\frac{Vne}{h} - F_{th}\right) * (l_2 - x_{in}), \tag{11}$$

$$\Delta\Phi + \Delta\mathrm{T} = \left(-\frac{Vne}{h} - F_{th}\right) * l, \tag{12}$$

Additions and modifications were made based on the classification discussed in Liu's study. If $\psi 1 - \frac{Z_p}{ne}[\Delta\Phi(x,y) + \Delta\mathrm{T}(x,y)] < \psi 1$, this indicates that the electric field force is less than the thermophoresis force, and some particles will settle onto the grounded electrode plate. By further increasing the voltage, the electric field force gradually offsets the thermophoresis force, and the normalized penetration efficiency Ω increases to 1. When $\psi 2 - \frac{Z_p}{ne}[\Delta\Phi(x,y) + \Delta\mathrm{T}(x,y)] \leq \psi 3$, Ω is 1, meaning that all particles pass through the EAC. When $\psi 1 - \frac{Z_p}{ne}[\Delta\Phi(x,y) + \Delta\mathrm{T}(x,y)] \geq 0\psi 3$, Ω is 0, meaning that all particles are captured by the high-voltage plate. If $\frac{Q_{sh}hne}{lw(neV+hF_{th})} < Z_p < \frac{(Q_{sh}+Q_a)hne}{lw(neV+hF_{th})}$, then the Eqs. (16) – (18) in Liu's study are modified to the following equations:

$$\Omega = \frac{\psi_3 - \left[\psi_1 - \frac{Z_p}{ne}(\Delta\Phi+\Delta\mathrm{T})\right]}{\psi_2 - \psi_1}, \tag{13}$$

$$P = max\left\{0, min\left[1{,}1 + \frac{Q_{sh}}{Q_a} - \frac{\left(Q_{sh} + {}^{Q_a}/_2\right)}{Q_a}\left(\frac{Z_p}{Z_{p,c}}\right)\right]\right\}0, \tag{14}$$

where P implies the transfer function of CS+EAC comprising the thermophoretic force. The central mobility, $Z_{p,c}$, corresponding to a 50% particle penetration efficiency, is calculated as follows:

$$Z_{p,c} = \frac{\left(Q_{sh} + {}^{Q_a}/_2\right)hne}{lw(neV_{50}+hF_{th})}, \tag{15}$$

https://doi.org/10.5194/egusphere-2026-565
Preprint. Discussion started: 5 March 2026

As shown in Eqs. (15), if the thermophoretic force points toward the ground plate, V_{50} increases compared to the case without thermophoretic force, which shifts the voltage-penetration efficiency curve to the right. Conversely, if the thermophoretic force points toward the high-voltage electrode, V_{50} decreases and the curve shifts to the left. The above is an analysis of the voltage-penetration efficiency function under ideal conditions. In fact, as shown in the simulation, the thermophoresis force acting on the particle changes as the particle moves. This results in the actual EAC transfer function lying between the two ideal analyses mentioned above. The estimated transfer function curve is such that as the voltage increases, the normalized penetration efficiency first rises, then plateaus, and finally decreases to zero.

2.3 Experimental setup

The study will characterize the performance of CS+EAC in terms of volatile particle removal efficiency and penetration efficiency of the CS, and transfer function of the EAC. The removal efficiency depends on the CS heating temperature, the size of the core catalyst, and the sample flow size entering the CS. The penetration efficiency experiments were conducted in two configurations: (i) CS+EAC without applied voltage, and (ii) CS+EAC with applied voltage. The transfer functions were carried out at various temperatures and dilution ratios. As shown in Fig. 3, the experimental setup includes a tube furnace and a soot particle generator for particle generation. The tube furnace generates tetracontane particles of controlled size by regulating the flow rate and heating temperature. The soot particle generator system comprises a mini-cast5 and a CS, which generate varying particle sizes by adjusting the flow ratios. The second configuration serves as the particle classification part, employing a DMA (TSI Model 3081) to classify monodisperse particles. These classifieds monodisperse particles then enter the experimental section consisting of three components: the bypass, the CS, and the CS+EAC, where the latter is equipped with an additional sheath flow supply. Finally, the PN and particle size distribution measurement section includes a Scanning Mobility Particle Sizer (SMPS) composed of a DMA (TSI Model 3081 or 3085) paired with a condensation particle counter (CPC, TSI Model 3788 or 3752) for particle size distribution analysis. The PN measurement unit consists of a separate CPC unit (TSI Model 3788 or 3752). Based on the experimental conditions, CPC-3788 was used in the removal efficiency experiment, and CPC-3752 was used in subsequent experiments. Analysis of the subsequent experimental results suggests that replacing the measuring device did not affect the research results. The specific experimental setup is shown in Fig. S1 to S4 in the supplementary materials.

https://doi.org/10.5194/egusphere-2026-565
Preprint. Discussion started: 5 March 2026

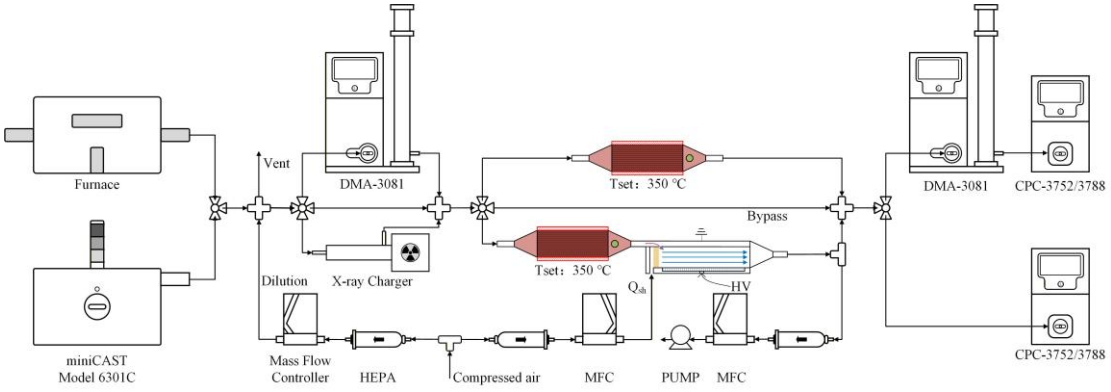

Figure 3: Experimental setup for evaluating the performance of CS+EAC.

2.3.1 Removal efficiency of volatile particles

This study first conducted some basic experiments, such as CS removal efficiency, to ensure that the research subjects met basic regulatory requirements. Tetracontane was selected to test the volatile particle removal efficiency of the CS due to its representative characteristics. According to Euro VI emission regulations, the VPR must achieve at least 99% removal of tetracontane particles measuring at least ≥30 nm, with a particle number concentration of ≥ 10E4 #/cm^3. The more stringent Euro VII regulation mandates that the VPR must remove more than 99.9% of tetracontane particles with a median particle size exceeding 50 nm and a mass concentration >1 mg/m^3. In this study, 0.3 g of tetracontane (Aladdin, >97.0% (GC)) was placed in a quartz boat at the center of a tube furnace. Tetracontane particles were generated by heating the tetracontane through the tube furnace, with their median particle size controlled by varying the heating temperature. In general, the RE declines gradually with increasing particle size and concentration, as well as with the reduced residence time in the CS. Therefore, this experiment was conducted under varying operational conditions, detailed in Table S1 and Fig. S1 in the supplementary materials.

The RE is expressed as follows:

$$RE = 1 - \frac{N_{CS}}{N_{bypass}}, \tag{16}$$

where N_{CS} refers to the number concentration of particles after the CS, and N_{bypass} indicates the number concentration of particles directly measured from the bypass. The experimental results are shown in Fig. S5-S6 in the supplementary materials.

2.3.2 Solid particle penetration experiments

Regulatory standards for VPR require testing penetration efficiency for solid particles with particle sizes of 15, 30, 50, and 100 nm. The penetration efficiency (f_p) is calculated as follows:

$$f_p = \frac{N_{CS+EAC}}{N_{bypass}} = \frac{1}{PCRF}, \tag{17}$$

where N_{CS+EAC} refers to the number concentration of particles after the CS+EAC, the particle concentration reduction factor (PCRF) is the reciprocal of the penetration efficiency. To obtain a complete penetration efficiency curve for the CS+EAC, some particle sizes were added to the experiments, and penetration efficiency experiments were conducted at different CS

https://doi.org/10.5194/egusphere-2026-565
Preprint. Discussion started: 5 March 2026

heating temperatures, different dilution ratios, and zero voltage. Table S2 shows the operating parameters for these experiments. The dilution ratio (DR) is calculated as follows:

$$DR = \frac{Q_{sh}+Q_{sa}}{Q_{sa}} = \frac{Q_t}{Q_{sa}}, \quad (18)$$

where Q_{sh} represents the sheath flow rate, Q_{sa} implies the sample flow rate, and Q_t signifies the total flow rate. The specific experimental setup is shown in Fig. S2 in the supplementary materials. In the experimental data graph presented in the results discussion, DR1 denotes a dilution ratio of 1, and so on.

2.3.3 Voltage-penetration efficiency curves for CS+EAC

Voltage-penetration efficiency curve test for the CS+EAC was evaluated relative to its zero-voltage penetration efficiency. The high-voltage source (Dong Wen High Voltage, China) used in the experiment operates within a range of 0 ~ -10000 V and includes an output voltage reading. The specific experimental setup is shown in Fig. S3 in the supplementary materials. Polydisperse particles with varying peak particle sizes were generated by adjusting the gas ratio in the soot generator. The soot particles initially pass through a CS (catalytic instruments, CS015) to remove volatile particles before entering the DMA-3081 for classification. The classified particles then enter the CS+EAC, where the applied high voltage in the EAC is increased linearly over a 120-s scanning cycle. The step voltage size was adjusted during the experiment. Each test comprised three consecutive scans, with the final voltage-penetration efficiency curve representing the average of the three measurements. In this study, the penetration efficiency curves were measured for particle sizes between 15 and 100 nm. The specific parameter settings are listed in Table S2.

2.3.4 Measurement of particle size distribution at different voltages

To validate the CS+EAC's capability for rough peak particle size estimation, experiments were conducted to measure the particle size distribution at varying step voltage under fixed operating conditions. The polydisperse particles generated by a soot generator were charged using soft X-rays before entering the CS+EAC. Particle size distribution measurements were recorded at different voltage settings and compiled into a trend graph. The specific experimental setup is shown in Fig. S4 in the supplementary materials. The peak particle size was determined by analyzing the decay rate of the particle number concentration alongside the V_{50} fit data. The experiments were conducted at 25 °C and 350 °C, with the 350 °C experiment highlighting improvements in the penetration efficiency more clearly.

2.3.5 Alternating measurement test at 10 or 23 nm

To assess the feasibility of PN interval measurement above 10 and 23 nm, the cut-off voltages for these measurements were first established through the experiments presented in Section 2.3.3. Subsequently, the high-voltage power supply was set to a square wave voltage of only 0 and -200 V, and the interval time was changed to study the effect of voltage changes on the stability and accuracy of concentration measurements, with the aim of determining the shortest accurate measurement interval. The experimental setup is shown in Fig. S3, with the operating parameters displayed in red. After classification, the 15 nm particles were subjected to CS+EAC and then measured for number concentration using CPC-3752. Changes in number concentration were observed by varying the interval time between 0 V and -200 V.

https://doi.org/10.5194/egusphere-2026-565
Preprint. Discussion started: 5 March 2026

3. Results and discussion

3.1 Penetration efficiency of CS+EAC without voltage

The experimental results presented in Fig. 4 indicate that, for a given DR, penetration efficiency decreases as the temperature increases to 350 °C. Notably, at 350 °C, the penetration efficiency improves with increasing DR. However, the efficiency for smaller particle sizes remains below regulatory requirements. Therefore, further enhancement of small particles is necessary for the CS+EAC system to meet the requirements at 350 °C.

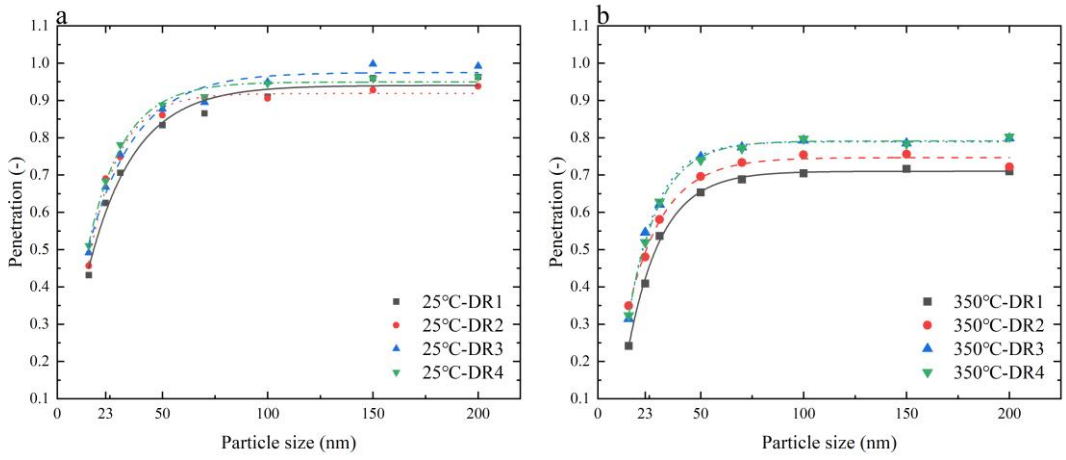

Figure 4: Particle penetration efficiency of CS+EAC at dilution ratios: (a) 25°C, and (b) 350°C.

3.2 Voltage-penetration efficiency curve

To characterize the voltage-particle penetration efficiency of the CS+EAC under different operating conditions. Based on the mechanical structure of CS+EAC, soot particles were used for the voltage-penetration efficiency experiments of EAC at different dilution ratios and temperatures. The experimental parameters are shown in Table S2, respectively. The flow rate was set with a sample flow rate Q_{sa} = 0.3 L/min and a sheath flow Q_{sh} ranging from 0 to 3 L/min.

3.2.1 Effect of temperature

Depending on the shape of the designed CS+EAC, the EAC will be heated due to its connection to the CS. Therefore, the voltage-penetration efficiency curve of the EAC is affected by the CS temperature. A key objective of this study is to investigate the extent to which an applied electric field can mitigate the thermophoretic loss of high-temperature particles. The maximum voltage of the EAC is limited to -5000 V, constrained by the narrow insulation distance between the high-voltage pole plate of the EAC and the adjacent metal structure. Figure 5 illustrates the normalized voltage-penetration efficiency curves of CS+EAC at different temperatures, with a dilution ratio of 4 (DR4). The vertical coordinate represents normalized penetration efficiency, calculated by dividing the penetration efficiency data from a single scan cycle by the penetration efficiency at 0V. The horizontal coordinate is the normalized voltage, where V_{50} refers to the voltage at which the normalized penetration efficiency is 50%. Above 250 °C, the particle penetration efficiency gradually increases with increasing voltage,

https://doi.org/10.5194/egusphere-2026-565
Preprint. Discussion started: 5 March 2026

indicating the effectiveness of applying the electric field force to resist the thermophoretic force to enhance the penetration efficiency. The maximum normalized penetration efficiency is positively correlated with CS temperature, with the normalized penetration efficiency of 23 nm at 350 °C increasing to around 1.2. Additionally, the descending portion of the voltage-penetration efficiency curve becomes steeper with increasing temperature. This may be due to the downward temperature gradient in the latter half of the classification zone, causing both the electric field force and thermophoretic force to point toward the high-voltage plate. Consequently, the particle penetration efficiency decreases at an accelerated rate, resulting in a steeper gradient. Moreover, as temperature increases, the downward thermophoretic force increases, further enhancing the steepness. Considering the operating temperature of the CS and the effectiveness of enhancing particle penetration efficiency, all subsequent voltage-penetration efficiency experiments were conducted at 350 °C.

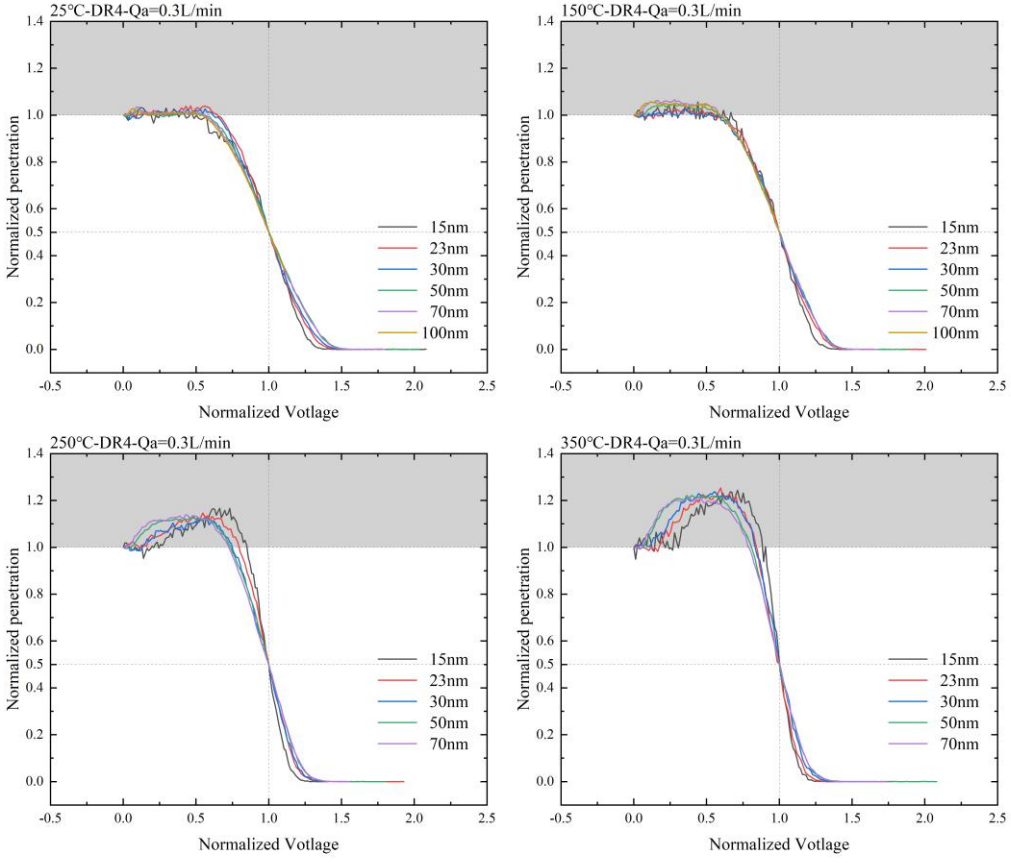

Figure 5: CS+EAC voltage-penetration efficiency curves at varying temperatures.

3.2.2 Effect of different dilution ratios

Figure 6a shows the normalized voltage-penetration efficiency curves at 350 °C for various dilution ratios. Consistent with theoretical predictions, the normalized penetration efficiency increases with increased voltage. As the voltage is further

https://doi.org/10.5194/egusphere-2026-565
Preprint. Discussion started: 5 March 2026

increased, the efficiency gradually decreases to 0. The maximum normalized penetration efficiency is positively correlated with the dilution ratio. When the dilution ratio exceeds 3, the maximum normalized penetration efficiency for each particle size is around 1.2. It is worth noting that the steepness decreases with increasing particle size at dilution ratio 1. The steepness of the curve increases significantly with increasing dilution ratio and the difference in steepness between particle sizes decreases gradually. This suggests that EAC requires a higher dilution ratio to reduce the effect of particle size on the consistency of the voltage-penetration efficiency curve. Figure S8 shows the voltage-penetration efficiency curve data for DR11, showing that the normalized curves for different particle sizes converge at high dilution ratios. This convergence indicates a gradual increase in the EAC's size resolution with increasing dilution ratio. However, it should be noted that as the total flow increases, the particle residence time within the EAC decreases, leading to a gradual increase in V_{50}. Considering this study's objective to mitigate the thermophoretic particle loss while acknowledging the EAC's maximum voltage limit of -5000 V, the final DR4 was chosen for the penetration efficiency enhancement experiments.

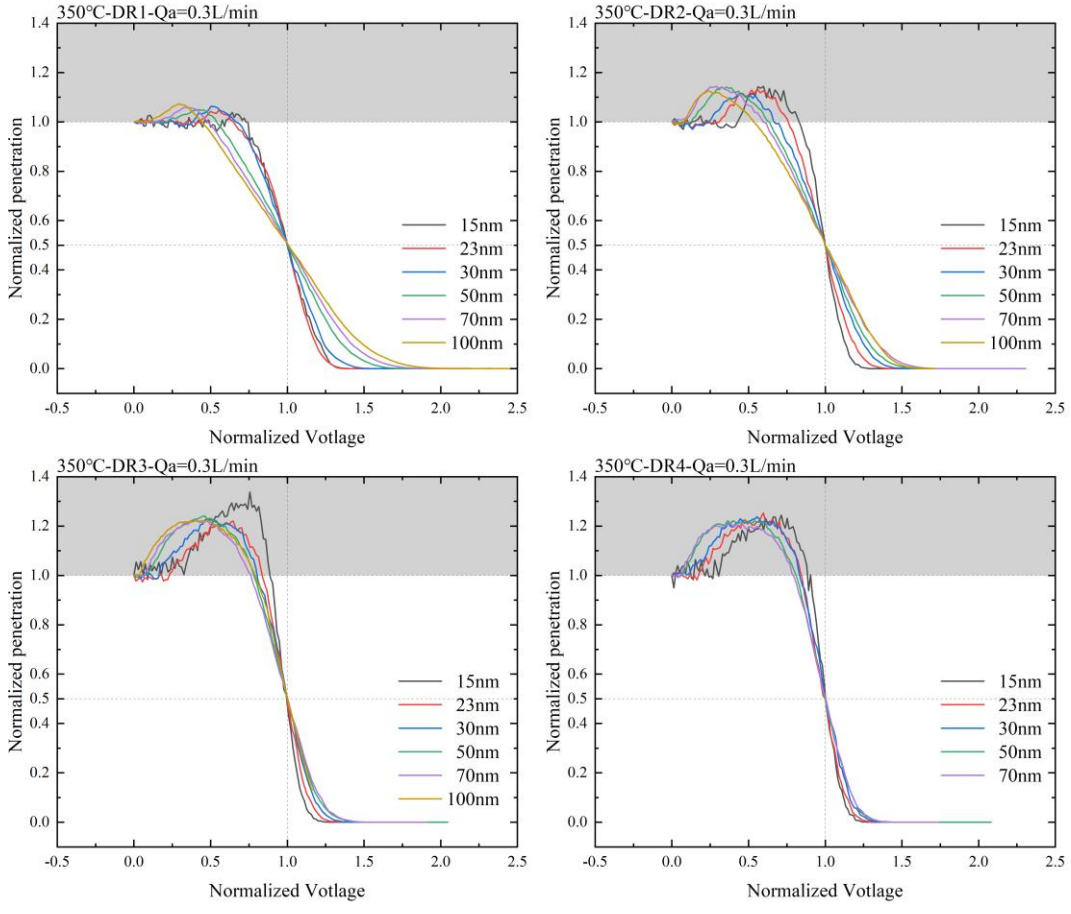

(a)

https://doi.org/10.5194/egusphere-2026-565
Preprint. Discussion started: 5 March 2026

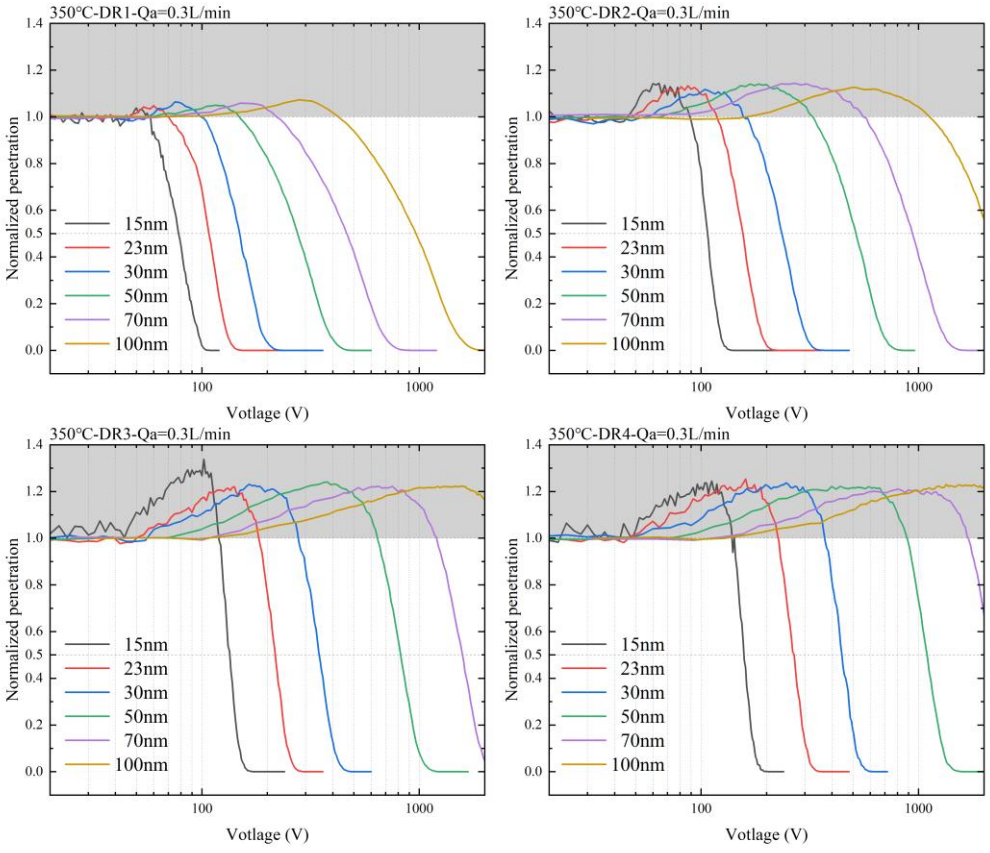

325

(b)

Figure 6: Voltage-penetration efficiency curves for CS+EAC under varying DRs: (a) normalized voltage, (b) applied voltage.

Figure 6b shows the normalized penetration efficiency curve under actual voltage conditions. To clearly illustrate changes in small particle size, the horizontal axis adopts a logarithmic scale. The complete data can be found in Fig. S7.

330 It can be seen that as the particle size increases, the voltage value corresponding to the highest penetration efficiency gradually increases. When selecting an appropriate voltage value, such as a lower voltage, the penetration efficiency of small particles with a diameter range of 15-30 nm can be improved, while the improvement ratio for large particles with a diameter range of 50-100 nm can be ignored. This indicates that by applying the appropriate voltage, the originally steep penetration efficiency curve can be flattened.

335 **3.2.3 The cutoff voltage, V_{50}**

Figure 7 presents the V_{50} values for various particle sizes across different temperatures and dilution ratios. The data indicate that the V_{50} increases progressively with the particle size and the DR. In Fig. 7b, the columns represent the fluctuation range of V_{50}, and the numbers represent the mean value of V_{50} under the same particle size and different temperature conditions.

https://doi.org/10.5194/egusphere-2026-565
Preprint. Discussion started: 5 March 2026

It can be seen that the impact of temperature on V_{50} remains within 10%. Particle size distribution measurements at different voltages will reference the V_{50} values derived from the fitted curves, as shown in Fig. 7.

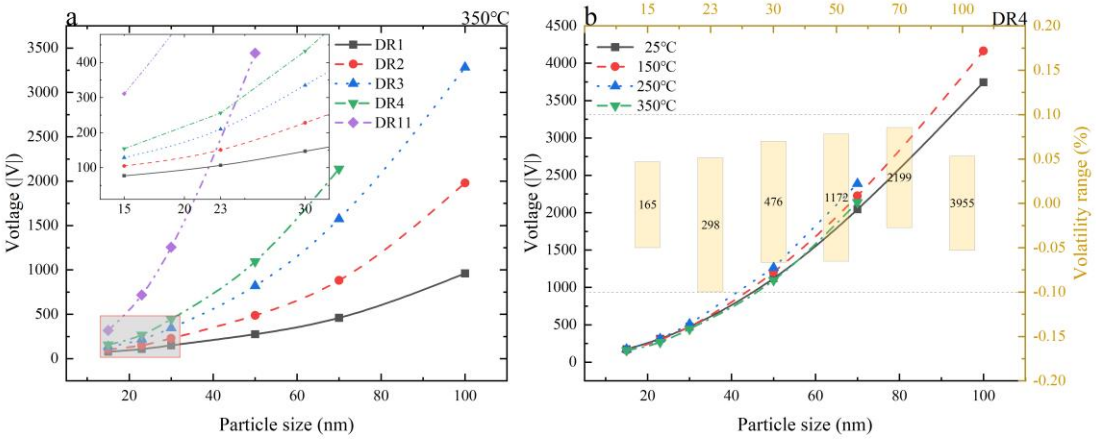

Figure 7: V_{50} at varying temperatures and DRs: (a) different DRs, and (b) varying temperatures. To clearly illustrate the fluctuation range of V_{50} at different temperatures for various particle sizes, the column chart (top horizontal axis) employs an equidistant scale, differing from the bottom horizontal axis.

3.3 Penetration efficiency improvement ratio and PCRF value

Using the voltage-penetration efficiency curves of the CS+EAC at 350 °C and a DR of 4, the voltage values of EAC corresponding to the peak penetration efficiency enhancement for small particle sizes (15, 23, and 30 nm) were selected. These voltages were then applied to determine the penetration efficiency enhancement ratios of particles across various particle sizes. From the voltage-penetration efficiency curve, the maximum penetration efficiency for 15 nm particles occurs at -112 V. Figure 8 presents the penetration efficiency enhancement ratios for various particle sizes at -112 V, showing a 24.4% increase for 15 nm particles. This improvement is based on the 350 °C-DR4 penetration efficiency data in Fig. 4b. The enhancement ratio decreases gradually as the particle size increases. This results in a flatter penetration efficiency curve for -112 V compared to 0 V. The PCRF value in the regulation is determined by the average of the penetration efficiencies for the three particle sizes 30 nm, 50 nm, and 100 nm (an additional 15nm penetration efficiency is added for the 10 nm regulation). The specific requirements and limits are shown in Fig. S9 (Giechaskiel, 2021).

A flatter penetration efficiency curve is essential for accurate PCRF determination, as the peak particle size is typically unknown during exhaust emission measurements. The optimal PCRF value is achieved when the penetration efficiencies across the relevant particle sizes are nearly uniform. As a result, the $PCRF_{15nm}$ at -112 V setting is suitable for 10 nm regulatory equipment and results in more accurate measurements. Further increasing the voltage to -160 V yields the maximum enhancement ratio for the 23 nm particles, reaching the value of 25.4%. However, the 55.5% reduction in penetration efficiency at 15 nm indicates that the -160 V setting is unsuitable for the latest 10 nm regulatory requirements. Excluding the 15 nm

https://doi.org/10.5194/egusphere-2026-565
Preprint. Discussion started: 5 March 2026

particles, the penetration efficiency curve at the -160 V setting is very flat, making it appropriate for 23 nm regulations. Table 1 summarizes the calculated PCRF values for the 10 and 23 nm regulations across various voltage settings. The data show that the PCRF value decreases as the penetration efficiency curve flattens out, thereby enhancing the accuracy of emission measurements.

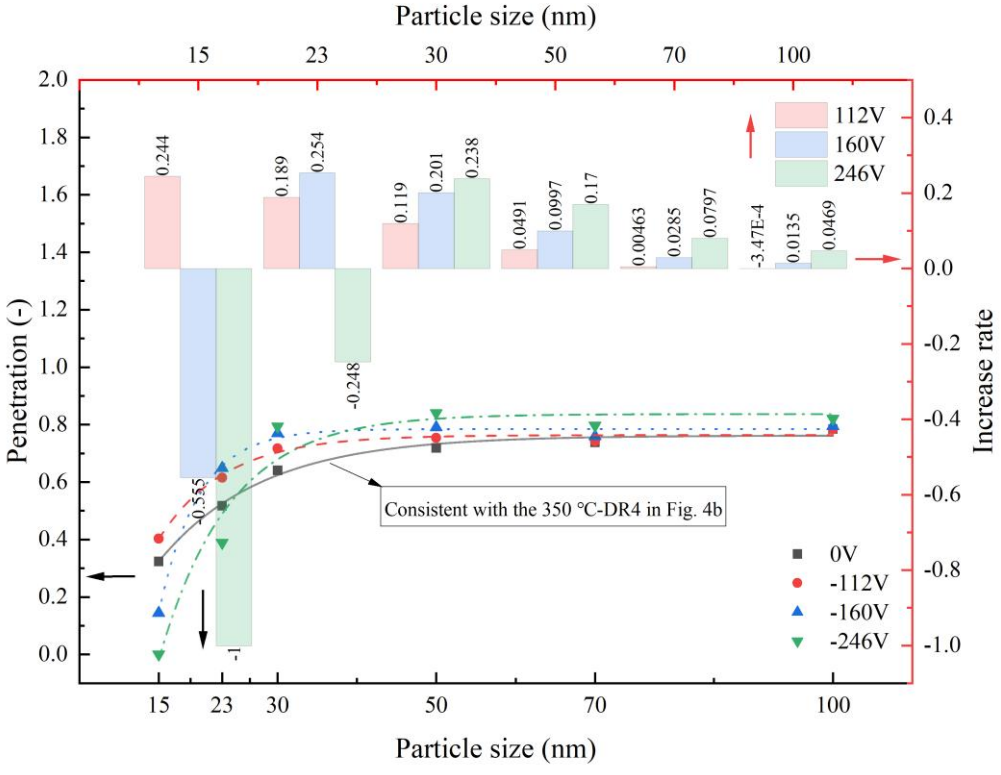

Figure 8: Penetration efficiency improvement ratio across various voltages. Arrows are used to indicate the coordinates of the penetration efficiency fitting curve and the improvement efficiency. To clearly illustrate the improvement rate in penetration efficiency across different particle sizes at varying voltages, the column chart (top horizontal axis) employs an equidistant scale, differing from the bottom horizontal axis.

Table 1

PCRF values at varying voltages.

	Penetration efficiency				$PCRF_{15nm}$	$PCRF_{23nm}$
	15 nm	30 nm	50 nm	100 nm		
0 V	32.36%	62.84%	73.99%	79.69%	1.822	1.399
-112 V_{15nm}	40.26%	70.31%	77.62%	79.66%	1.612	1.322
-160 V_{23nm}	14.41%	75.44%	81.37%	80.76%	2.683	1.264
-246 V_{30nm}	0.00%	77.78%	86.55%	83.42%	-	1.213

https://doi.org/10.5194/egusphere-2026-565
Preprint. Discussion started: 5 March 2026

3.4 Particle size distribution and response time

To validate the ability of the CS+EAC to determine the peak particle size of the particle size distribution with short time and coarse resolution, the performance of CS+EAC is assessed through both the particle size distribution analysis and the concentration-time response evaluation.

3.4.1 Particle size distribution and peak particle size at stepping voltage

Using the voltage-penetration efficiency curves of CS+EAC obtained from Section 3.3 and the V_{50} data, we simulated motor vehicle exhaust by generating soot particles and examined how the particle size distribution changed with varying voltages. Figure 9a illustrates the particle size distributions of CS+EAC at 25 °C under varying voltages. The soot particles with an initial peak size of 35 nm shifted to a peak size of 37.2 nm after passing through the CS+EAC at 0 V. This shift occurs because the penetration efficiency increases with increasing particle size, resulting in a greater reduction in the concentration of small-sized particles. As the voltage increases, it can be seen that the particle size distribution is gradually removed from left to right. This is determined by the transfer function of CS+EAC, where higher dilution ratios theoretically lead to a more vertical cut on the left side of the particle size distribution. By continuously increasing the voltage and calculating the PN reduction rate, the voltage corresponding to the fastest decline—denoted as V_{50}—identifies the peak particle size within the measured distribution. The scatter plot of the total concentration at varying voltages in Fig. 9a shows the steepest decline near -700 V. Correspondingly, the particle size distribution indicates that the number concentration of peak particle size (37.2 nm) is approximately halved at -700 V compared to that at 0 V. This indicates that when V_{50} is -700 V, the corresponding particle size is the peak particle size of the measured polydisperse particles, which is verified by Fig. 7, where 37.2 nm corresponds to a V_{50} around -700 V.

https://doi.org/10.5194/egusphere-2026-565
Preprint. Discussion started: 5 March 2026

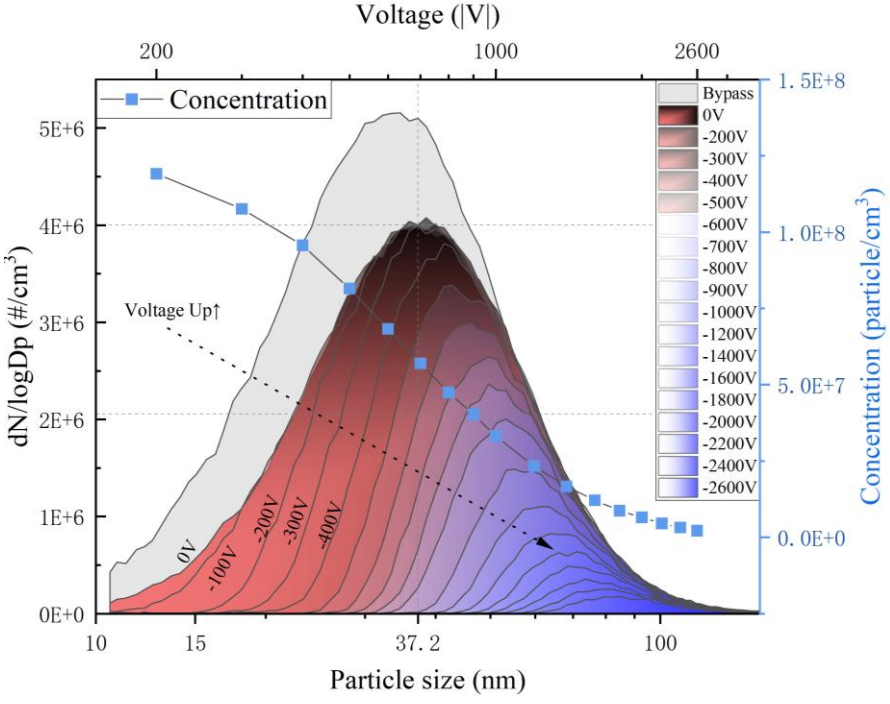

(a)

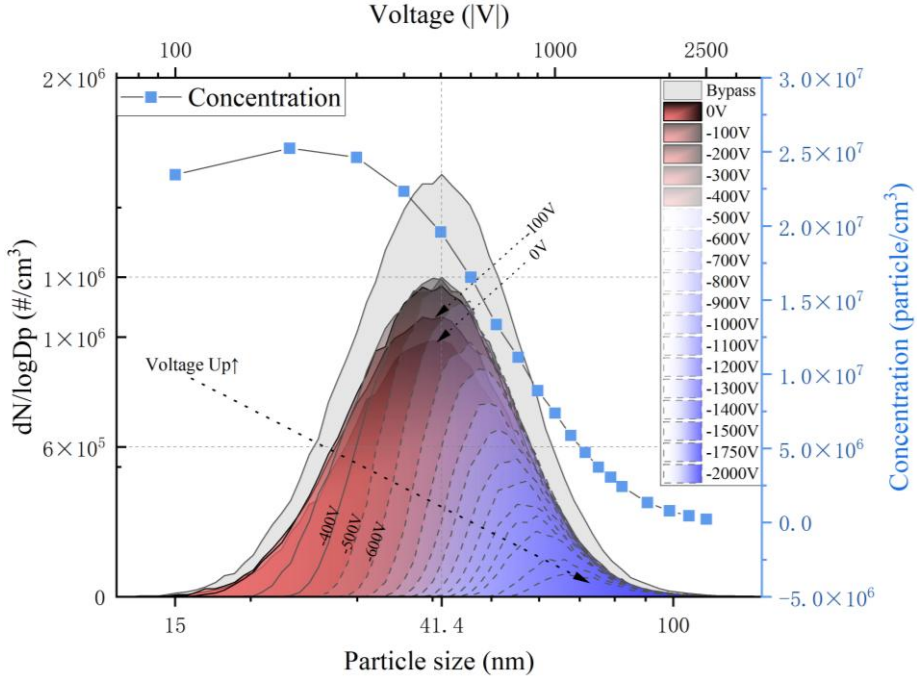

(b)

Figure 9: Particle size distribution measurements of CS+EAC at stepped voltages: (a) 25 °C, and (b) 350 °C.

https://doi.org/10.5194/egusphere-2026-565
Preprint. Discussion started: 5 March 2026

Further, the same experiment was repeated at 350 °C. Based on the transfer function at this temperature and a DR of 4, CS+EAC is expected to show an initial increase followed by a decrease in the peak particle size concentration as voltage increases. Figure 9b shows that the number concentration of the particle size distribution increases with increasing voltage, but the peak particle size does not change much. As the voltage increases further, the particle size distribution concentration gradually shifts and decreases from left to right. At voltages from -600 V to -700 V, the peak particle size concentration of the initial particle size distribution is reduced by half, which indicates that the V_{50} corresponding to the peak particle size is within the range of this voltage interval. Similarly, comparison with the V_{50}-particle size fitting curves in Fig. 7 confirms that the above method for the approximate estimation of peak particle size is both feasible and effective.

3.4.2 Cycle voltage and particle concentration response time

Based on the transfer function characteristics of CS+EAC, alternate measurements with 10 nm or 23 nm as D_{50} are possible. D_{50} is the particle size for which the counting efficiency in the emission measurement system is 50%. In practical applications, measurement must be made within seconds, as particle concentrations and size distributions vary in real-time. Therefore, time resolution is critical for alternating measurements. To maintain effective classification, the voltage conversion time must be rapid yet controlled. For CS+EAC, the key to achieving particle size classification conversion is the steady rate of voltage conversion and the residence time of particle in the EAC classification region. This is related to the response time of the voltage control module and the flow through the EAC. Based on the above research and analysis, it is proposed to carry out the 0~-200 V voltage conversion concentration measurement of soot particles with a particle size of 15 nm under the conditions of sample flow of 0.3 L/min, 350 °C, and a dilution ratio of 4. The experimental results are shown in Fig. 10. Experiments were conducted by setting different intervals to determine the time required for concentration stabilization. When t =1 s, the voltage failed to accurately switch to 0 V or -200 V. This caused the voltage to remain at an in-between value, thereby preventing the complete removal of particles. As t increases to 5 seconds, the 15 nm particles are completely removed. Notably, when the voltage switches to 0 V, the concentration exceeds the average value. This may be due to the slower discharge rate of the high-voltage source, thereby improving the penetration efficiency of the particles. In actual measurements, precise concentration measurements can be achieved by reading the voltage corresponding to the peak concentration and combining it with the PCRF value associated with that voltage. We can see from the end of the measurement that the concentration gradually decreases to the average value. Therefore, by using a custom voltage source, interval measurements can be achieved when the switching time is larger than 5 seconds. This measurement method can evaluate the concentration percentage of particles from 10 to 23 nm in the exhaust gas.

https://doi.org/10.5194/egusphere-2026-565
Preprint. Discussion started: 5 March 2026

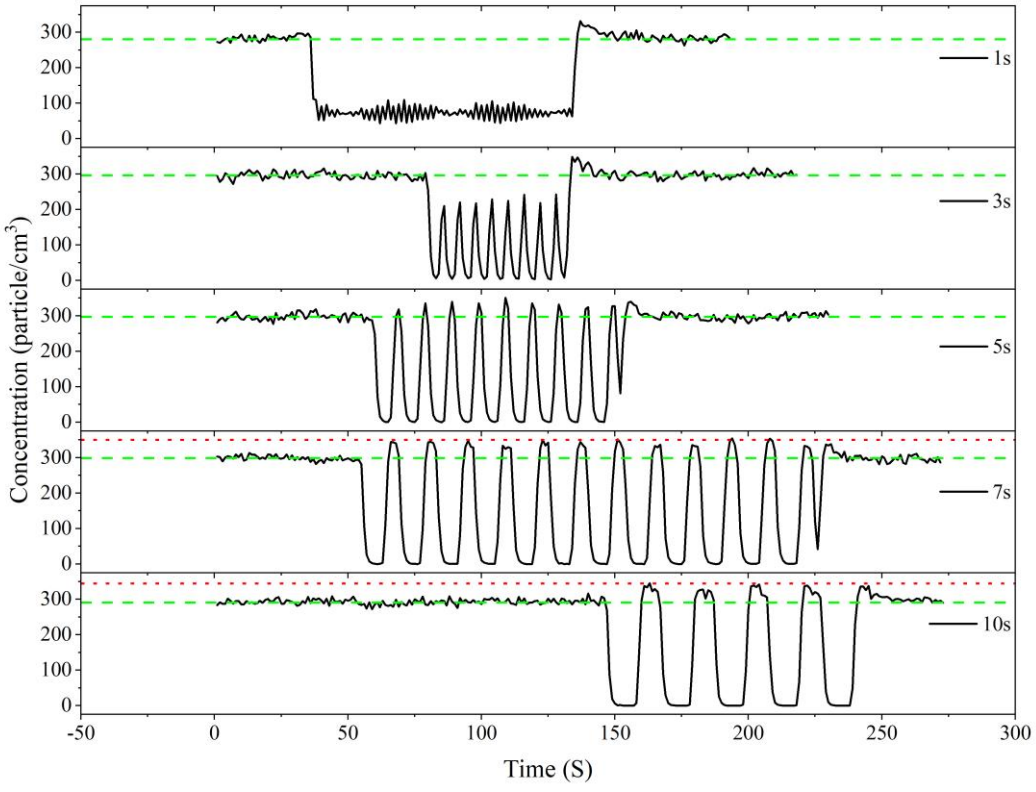

425

Figure 10: Soot particle concentration measurements with a particle size of 15 nm at varying transition time intervals.

4. Conclusion

In order to further improve the penetration efficiency without decreasing the volatile particle removal efficiency of the CS, this study designs a device that integrates CS with a plate EAC. The charged particles heated by the CS enter directly into the
430 EAC, where the electric field force counteracts the thermophoretic force, thereby further improving the particle penetration efficiency. The performance test was carried out in two parts: the first part involved measuring the removal efficiency of the CS, and the second part focused on assessing the penetration efficiency without voltage and obtaining the voltage-penetration efficiency curves for the CS+EAC. Using the voltage–penetration curves of CS+EAC, the particle size distribution measurements and PCRF calculations were conducted at various voltages. Further, alternating measurements of the number
435 concentration for particle size intervals above 10 and 23 nm were performed by periodically adjusting the EAC voltage value.

Experimental data demonstrate that the CS achieves an exceptionally high removal efficiency of volatile particles. At a flow rate of 1.5 L/min, the removal efficiency of tetracontane particles with a peak particle size of 88 nm and a mass concentration above 1 mg/m^3 was greater than 99.99%. Moreover, lowering the flow rate further enhanced the removal efficiency. CS+EAC uses sheath flow to dilute and cool the sample flow, resulting in particle penetration efficiencies of 32.3% for 15 nm particles

https://doi.org/10.5194/egusphere-2026-565
Preprint. Discussion started: 5 March 2026

and 79.6% for 100 nm particles (at a sample flow of 0.3 L/min, DR of 4, and CS temperature of 350 °C). Penetration efficiency will be higher with dilution compared to undiluted. Voltage-penetration efficiency curve demonstrates that applying an electric field can increase particle penetration efficiency by counteracting the thermophoretic force, which is manifested as a hump in the voltage-penetration efficiency curve. This improvement becomes more pronounced with higher DR and temperatures. Increasing the DR raises the V_{50} value and sharpens the descending slope of the curve, while temperature has a smaller effect on V_{50}.

Based on the voltage-penetration efficiency curves for CS+EAC operating at 350 °C—with a sample flow of 0.3 L/min and a DR of 4—multiple voltage values were chosen to calculate the PCRF. At -112 V, the penetration efficiency for 15 nm particles is improved by 24.4%, while the efficiency for 100 nm particles remains nearly unchanged, resulting in a flattened penetration efficiency curve. In emission particle measurements, the PCRF values derived from such a smoother curve result in more accurate measurements. Further increasing the voltage to -200 V produced a penetration efficiency curve suitable for 23 nm regulatory devices. To explore the feasibility of alternating number concentration measurements for particle size intervals above 10 or 23 nm, periodic measurements were performed at two set classification voltages. When the interval time was at least 5 s ($T \geq 5$ s), the maximum value obtained from the interval measurement closely matched the actual measurement value. Under these conditions, the CS+EAC combined with the particle counting device can accurately measure different particle size intervals.

Finally, this study demonstrates that CS+EAC provides the following functions:

i) It dilutes the aerosol to meet measurement equipment requirements.

ii) It improves the particle penetration efficiency without decreasing the removal efficiency of the volatile particles.

iii) It improves the PCRF value of the pretreatment device, resulting in more accurate measurements of the particle number concentrations in emissions.

iv) It enables concentration measurements of numbers in different particle size bands such as 15 nm/23 nm and above will be realized, which will help to roughly locate the peak particle size of the emission during the field test.

It is worth noting that this study did not conduct experiments combining unipolar diffusion chargers, which means that some work still needs to be done before the study can be put into practical use. Next, we will explore the effectiveness of this study in practical applications by combining it with highly efficient unipolar diffusion chargers.

Acknowledgements

This work was supported by the Jing-Jin-Ji Regional Integrated Environmental Improvement-National Science and Technology Major Project of Ministry of Ecology and Environment of China (No. 2025ZD1201200); the Research Team Construction Project of Hefei Comprehensive Science Center Environmental Research Institute (HYKYTD2024006); the National Key Research and Development Program of China (2023YFC3705400); the National Natural Science Foundation of

https://doi.org/10.5194/egusphere-2026-565
Preprint. Discussion started: 5 March 2026

China (42005108 and U2133212) and Open Fund Project of the Key Laboratory of Motor Vehicle Pollution Control and Simulation of the State Environmental Protection Administration (Grant No. VECS2021S05).

References

Amanatidis, S., Ntziachristos, L., Karjalainen, P., Saukko, E., Simonen, P., Kuittinen, N., Aakko-Saksa, P., Timonen, H., Rönkkö, T., & Keskinen, J.: Comparative performance of a thermal denuder and a catalytic stripper in sampling laboratory and marine exhaust aerosols. Aerosol Sci. Technol., 52(4), 420–432, 2018. https://doi.org/10.1080/02786826.2017.1422236

Babar, Z. Bin, Ashraf, F., Park, J. H., & Lim, H. J.: Volatility parameters of secondary organic aerosol components determined using a thermal denuder. Atmos. Environ, 226(March), 117405, 2020. https://doi.org/10.1016/j.atmosenv.2020.117405

Burtscher, H., Baltensperger, U., Bukowiecki, N., Cohn, P., Hüglin, C., Mohr, M., Matter, U., Nyeki, S., Schmatloch, V., Streit, N., & Weingartner, E.: Separation of volatile and non-volatile aerosol fractions by thermodesorption: Instrumental development and applications. J. Aerosol Sci, 32(4), 427–442, 2001. https://doi.org/10.1016/S0021-8502(00)00089-6

Centre.; I. For, J. R.; Transport, E.; Giechaskiel, B.; Martini, G. Review on Engine Exhaust Sub-23nm Solid Particles. Publications Office, 2014. https://doi.org/10.2790/22597.

Chen, X., Liu, Q., Jiang, J., & Chen, D. R.: Performance evaluation of a circular electrical aerosol classifier (CirEAC). J. Aerosol Sci, 118(February), 100–110, 2018. https://doi.org/10.1016/j.jaerosci.2018.02.003

D. Park, Kim, S., Choi, N. K., & Hwang, J.:Development and performance test of a thermo-denuder for separation of volatile matter from submicron aerosol particles. J. Aerosol Sci, 39(12), 1099–1108, 2008. https://doi.org/10.1016/j.jaerosci.2008.07.002

Faulhaber, A. E., Thomas, B. M., Jimenez, J. L., Jayne, J. T., Worsnop, D. R., & Ziemann, P. J.: Characterization of a thermodenuder-particle beam mass spectrometer system for the study of organic aerosol volatility and composition. Atmos. Meas. Tech, 2(1), 15–31, 2009. https://doi.org/10.5194/amt-2-15-2009

Fierz, M., Vernooij, M. G. C., & Burtscher, H.: An improved low-flow thermodenuder. J. Aerosol Sci, 38(11), 1163–1168, 2007. https://doi.org/10.1016/j.jaerosci.2007.08.006

Giechaskiel, B.: Differences between tailpipe and dilution tunnel sub-23 nm nonvolatile (solid) particle number measurements. Aerosol Sci. Technol, 53(9), 1012–1022, 2019. https://doi.org/10.1080/02786826.2019.1623378

Giechaskiel, B., & Drossinos, Y.: Theoretical investigation of volatile removal efficiency of particle number measurement systems. SAE Tech. Pap, April, 1140–1151, 2010. https://doi.org/10.4271/2010-01-1304

Giechaskiel, B., Maricq, M., Ntziachristos, L., Dardiotis, C., Wang, X., Axmann, H., Bergmann, A., & Schindler, W.: Review of motor vehicle particulate emissions sampling and measurement: From smoke and filter mass to particle number. J. Aerosol Sci, 67, 48–86, 2014. https://doi.org/10.1016/j.jaerosci.2013.09.003

https://doi.org/10.5194/egusphere-2026-565
Preprint. Discussion started: 5 March 2026

Giechaskiel, B., & Martini, G.: PMP: Sub 23 nm review. PMP informal document, GRPE-PMP-28-02. ⟨https://www2.unece.org/wiki/download/ attachments/15761626/GRPE-PMP-28-02%20PMP%20sub23nm.pdf?api=v2⟩ Accessed 08.07.14. 2013.

Giechaskiel, B., & Martini, G.: Review on engine exhaust sub-23 nm particles DRAFT. 2014

Giechaskiel, B., Melas, A. D., Lähde, T., & Martini, G.: Non-Volatile Particle Number Emission Measurements with Catalytic Strippers: A Review. Vehicles, 2(2), 342–364, 2020. https://doi.org/10.3390/vehicles2020019

Giechaskiel, B., Melas, A., Martini, G., & Dilara, P.: Overview of vehicle exhaust particle number regulations. Processes, 9(12), 1–25, 2021. https://doi.org/10.3390/pr9122216

Hinds, W. C.: Aerosol technology : properties, behavior, and measurement of airborne particles. 2nd ed. New York (N.Y.): Wiley. 1999.

Hooftman, N., Messagie, M., Van Mierlo, J., & Coosemans, T.: A review of the European passenger car regulations – Real driving emissions vs local air quality. Renew. Sustain. Energy Rev., 86(July 2017), 1–21, 2018. https://doi.org/10.1016/j.rser.2018.01.012

Huffman, J. A., Ziemann, P. J., Jayne, J. T., Worsnop, D. R., & Jimenez, J. L.: Development and characterization of a fast-stepping/scanning thermodenuder for chemically-resolved aerosol volatility measurements. Aerosol Sci. Technol., 42(5), 395–407, 2008. https://doi.org/10.1080/02786820802104981

Knutson, E. O., & Whitby, K. T.: Aerosol classification by electric mobility: apparatus, theory, and applications. J. Aerosol Sci., 6(6), 443-451, 1975.

Liu, X., Bai, X., Tian, H., Wang, K., Hua, S., Liu, H., Liu, S., Wu, B., Wu, Y., Liu, W., Luo, L., Wang, Y., Hao, J., Lin, S., Zhao, S., & Zhang, K.: Fine particulate matter pollution in North China: Seasonal-spatial variations, source apportionment, sector and regional transport contributions. Environ. Res., 184(March), 109368, 2020. https://doi.org/10.1016/j.envres.2020.109368

Liu, Q., & Chen, D. R.: Performance evaluation of a miniature plate Electrostatic Aerosol Analyzer (mini-plate EAA). J. Aerosol Sci., 95, 30–42, 2016. https://doi.org/10.1016/j.jaerosci.2016.01.001

Liu, B. Y. H., & Pui, D. Y. H.: On the performance of the electrical aerosol analyzer. J. Aerosol Sci., 6, 249–264, 1975.

Liu, B. Y. H. , Pui, D. Y. H. , & Kapadia, A.: Electrical aerosol analyzer: history, principle, and data reduction. engineering. 1976.

Louvaris, E. E., Karnezi, E., Kostenidou, E., Kaltsonoudis, C., & Pandis, S. N.: Estimation of the volatility distribution of organic aerosol combining thermodenuder and isothermal dilution measurements. Atmos. Meas. Tech., 10(10), 3909–3918. (2017). https://doi.org/10.5194/amt-10-3909-2017

Melas, A. D., Koidi, V., Deloglou, D., Daskalos, E., Zarvalis, D., Papaioannou, E., & Konstandopoulos, A. G.: Development and evaluation of a catalytic stripper for the measurement of solid ultrafine particle emissions from internal combustion engines. Aerosol Sci. Technol., 54(6), 704–717. (2020).https://doi.org/10.1080/02786826.2020.1718061

https://doi.org/10.5194/egusphere-2026-565
Preprint. Discussion started: 5 March 2026

Mendes, L., Eleftheriadis, K., & Biskos, G. Performance comparison of two thermodenuders in Volatility Tandem DMA measurements. J. Aerosol Sci., 92, 38–52. (2016). https://doi.org/10.1016/j.jaerosci.2015.10.002

Rönkkö, T., Pirjola, L., Ntziachristos, L., Heikkilä, J., Karjalainen, P., Hillamo, R., & Keskinen, J.: Vehicle engines produce exhaust nanoparticles even when not fueled. *Environ. Sci. Technol.*, *48*(3), 2043–2050. (2014). https://doi.org/10.1021/es405687m

Stevanovic, S., Miljevic, B., Madl, P., Clifford, S., & Ristovski, Z.: Characterisation of a commercially available thermodenuder and diffusion drier for ultrafine particles losses. *Aerosol Air Qual. Res.*, 15(1), 357–363. (2015).https://doi.org/10.4209/aaqr.2013.12.0355

Swanson, J., & Kittelson, D.: Evaluation of thermal denuder and catalytic stripper methods for solid particle measurements. *J. Aerosol Sci.*, 41(12), 1113–1122. (2010). https://doi.org/10.1016/j.jaerosci.2010.09.003

Swanson, J., Kittelson, D., Giechaskiel, B., Bergmann, A., & Twigg, M.: A miniature catalytic stripper for particles less than 23nanometers. *SAE Tech. Pap.*, 2, 542–551. (2013). https://doi.org/10.4271/2013-01-1570

Talbot, L., Cheng, R. K., Schefer, R. W., & Willis, D. R. Thermophoresis of particles in a heated boundary layer. *J. Fluid Mech., 101*(4), 737–758. (1980). https://doi:10.1017/S0022112080001905

Wehner, B., Philippin, S., & Wiedensohler, A.: Design and calibration of a thermodenuder with an improved heating unit to measure the size-dependent volatile fraction of aerosol particles. *J. Aerosol Sci.*, 33(7), 1087–1093. (2002). https://doi.org/10.1016/S0021-8502(02)00056-3

Whitby, K. T., & Clark, W. E.: Electric aerosol particle counting and size distribution measuring system for the 0.015 to 1 μ size range. *Tellus*, *18*(2–3), 573–586. (1966). https://doi.org/10.3402/tellusa.v18i2-3.9340

Woo, M., Giannopoulos, G., Rahman, M. M., Swanson, J., Stettler, M. E. J., & Boies, A. M.: Multiscale numerical modeling of solid particle penetration and hydrocarbons removal in a catalytic stripper. *Aerosol Sci. Technol.*, 55(9), 987–1000. (2021).https://doi.org/10.1080/02786826.2021.1909700

Xie, Z., Gui, H., Zhang, J., Yang, B., Kang, S., Wei, X., Yu, T., Yang, Y., Liu, J., & Liu, W.: Measurement techniques new progress of atmospheric fine particles. *Energy Environmental Protection,* 37(2): 16-29. (2023). https://doi:10.20078/j.eep.20230308.